



Published in final edited form as:

Cancer Gene Ther. 2022 October ; 29(10): 1463–1476. doi:10.1038/s41417-022-00454-5.

TMPRSS2-ERG promotes the initiation of prostate cancer by suppressing oncogene-induced senescence

Lei Fang¹, Dongmei Li², JuanJuan Yin¹, Hong Pan³, Huihui Ye⁴, Joel Bowman¹, Brian Capaldo¹, Kathleen Kelly^{1,*}

¹Laboratory of Genitourinary Cancer Pathogenesis, National Cancer Institute, Bethesda, Maryland

²Immunology and Reproduction Biology Laboratory & State Key Laboratory of Analytical Chemistry for Life Science, Medical School, Nanjing University, Nanjing, Jiangsu, P.R.China

³Department of Oncology, Zhejiang Provincial Hospital of Traditional Chinese Medicine, Hangzhou, Zhejiang, P.R.China

⁴Department of Pathology and Department of Urology, University of California Los Angeles, Los Angeles, California

Abstract

ERG translocations are commonly involved in the initiation of prostate neoplasia, yet previous experimental approaches have not addressed mechanisms of oncogenic inception. Here, in a genetically-engineered mouse model, combining *TMPRSS2*-driven *ERG* with *Kras*^{G12D} led to invasive prostate adenocarcinomas, while *ERG* or *Kras*^{G12D} alone were non-oncogenic. In primary prostate luminal epithelial cells, following inducible oncogenic *Kras* expression or *Pten* depletion, *TMPRSS2-ERG* suppressed oncogene-induced senescence, independent of TP53 induction and RB1 inhibition. Oncogenic KRAS and *TMPRSS2-ERG* synergized to promote tumorigenesis and metastasis of primary luminal cells. The presence of *TMPRSS2-ERG* compared to a wild-type background was associated with a stemness phenotype and with relatively increased RAS-induced differential gene expression for MYC and mTOR-regulated pathways, including protein translation and lipogenesis. In addition, mTOR inhibitors abrogated ERG-dependent senescence resistance. These studies reveal a previously unappreciated function whereby ERG expression primes preneoplastic cells for the accumulation of additional gene mutations by suppression of oncogene-induced senescence.

Users may view, print, copy, and download text and data-mine the content in such documents, for the purposes of academic research, subject always to the full Conditions of use: <https://www.springernature.com/gp/open-research/policies/accepted-manuscript-terms>

*corresponding author: Kathleen Kelly, Building 37 Room 1068 9000 Rockville Pike Bethesda MD 20892; kellyka@mail.nih.gov; phone: 240-760-6827; FAX: 240-541-4503.

Author contributions

L.F. and K.K. conceived and designed the original research plans and supervised the research. L.F., D.L. and H.P. performed the experiments. J.Y. performed *in vivo* orthotopic and intracardiac injections and supervised bioluminescent imaging of tumor growth. H.Y. performed histological analysis of triple transgenic mice and evaluated IHC staining results. J.B. and B.C. analyzed RNA-seq data. L.F. and K.K. wrote the manuscript with contributions from all authors.

Conflict of interest: the authors declare no competing interests.

Introduction:

Prostate cancer is the most common non-cutaneous cancer diagnosed in men. For Caucasian men, the most frequent genetic alteration in prostate cancer is overexpression of the Ets transcription factor ERG, usually as a result of chromosomal translocation adjacent to the *TMPRSS2* promoter¹. The high occurrence of *TMPRSS2-ERG* translocations in primary prostate cancer as well as their presence in the earliest pathologically defined neoplastic lesions support a role for ERG overexpression in prostate cancer initiation^{2,3}. A mechanistic understanding for the role of ERG in the preneoplastic to neoplastic transition has been elusive, in part due to a lack of appropriate models.

ERG is a tissue-specific transcription factor necessary for the maintenance, function, and differentiation of adult hematopoietic stem cells and for the development and maintenance of endothelial cell derived vasculature^{4,5}. A single role for ectopic ERG in prostate cancer has not been clearly established and may in fact vary depending upon the stage of prostate cancer development⁶. ERG-mediated transcription is context dependent as a result of interactions with other transcription factors, competition with ETS transcription factor family members, and post-transcriptional regulation. In addition, ERG chromatin binding is dependent upon interaction with the chromatin remodeling BAF complex⁷, suggesting that ERG may broadly influence gene expression through epigenetic as well as direct transcriptional mechanisms.

In the *TMPRSS2-ERG*-expressing VCaP prostate cancer cell line, depletion of ERG reduced tumorigenicity, migration, and luminal differentiation markers^{8,9}. In HPV18-immortalized RWPE prostate epithelial cells, ectopic ERG expression increased migration and clonogenicity¹⁰. Thus, in long-term human cell lines, ERG expression promotes growth and invasiveness. In mouse models, ERG expression results in changes to primary prostate cells including an increased frequency of self-renewing stem/progenitor cells¹¹ and a TP63 down regulation-dependent, AR-independent basal to luminal differentiation shift in tissue-derived organoids¹². Ectopic ERG expression alone is associated with no or minimal histological changes in transgenic prostate tissue and no appreciable, consistent gene expression changes among various models¹³⁻¹⁵.

Previously, we generated a bacterial artificial chromosome encoded *TMPRSS2-ERG* transgenic mouse model in which the *TMPRSS2-ERG* fusion protein is driven by the *TMPRSS2* promoter¹¹, recapitulating the chromosomal architecture encompassing the regulatory elements present in human prostate cancer. Crossing this *TMPRSS2-ERG* model with a prostate epithelial specific *Pten* deletion model accelerated the appearance, but not the progression, of *Pten*^{+/-} dependent early (mPIN) lesions in an FVB background, consistent with a similar study¹⁴. By contrast in the C57BL/6 background, probasin (*Arr2pb*)-driven non-fusion ERG led to progression of advanced *Pten*^{+/-} lesions¹³. These data suggest that *Erg* overexpression and *Pten* heterozygous loss synergize in early lesion formation and that ERG can contribute to additional tumor progression in sufficiently advanced neoplasia¹⁶. Thus, ERG function appears to be pleiotropic and context dependent, which suggests potentially distinct contributions depending upon the underlying genomic landscape and stage of prostate cancer development.

Here we show *TMPRSS2-ERG* synergy with *K-Ras^{G12D}* initiated in vivo oncogenesis, but not with *Tp53* deletion. Using primary prostate luminal epithelial cultures, we interrogated cell-intrinsic mechanisms of ERG-dependent transformation and observed a significant effect of ERG expression on inhibition of oncogene-induced senescence (OIS). Senescence is a stress-induced, persistent cell cycle arrest status, which occurs in a variety of physiological and pathological processes¹⁷. Cellular senescence is best known as a tumor suppressive mechanism that occurs following oncogenic activation¹⁸. OIS is thought to occur when cells receive a pro-mitogenic signal with simultaneous anti-proliferative signals. Although senescence is often executed by constitutive activation of the growth suppressive CDKN2A-RB1 and/or TP53 pathways, mechanisms do not seem to be universal across cell types and genetic contexts¹⁹. We provide evidence that ERG expression in preneoplastic prostate luminal cells is one of the earliest selected genomic mutations in prostate cancer as a result of its contextual function that allows evasion of oncogene-induced senescence.

Results:

***TMPRSS2-ERG* synergized with *Kras^{G12D}* to promote invasive adenocarcinoma in an *in vivo* mouse model**

Previously we reported in a genetically engineered mouse models that *TMPRSS2-ERG* transgenesis synergizes with heterozygous *Pten* deletion, but not with deletion of another early prostate cancer mutation, *Nkx3.1*, to accelerate the development of prostatic intraepithelial neoplasia (PIN) in mice¹¹. To interrogate the interaction of ERG with fundamental pathways that mediate oncogenesis through regulating growth and differentiation signaling networks, we crossed *TMPRSS2-ERG* transgenic mice with *Pb-CRE* driven conditional *Tp53* deletion or oncogenic Ras (LSL *Kras^{G12D}*) induction models. Prostate lobes and urogenital organs from triple transgenic mice (*TMPRSS-ERG+;Pb-Cre4+;Kras^{G12D/+}* or *Tp53-/-*) were compared at 6 months and 1 year to double transgenic littermates (*Pb-Cre4+; Kras^{G12D/+}* or *Tp53-/-*) without the *TMPRSS-ERG* transgene. There were no neoplastic changes observed in *TMPRSS-ERG+;Pb-Cre4+;Tp53-/-* –prostates. However, at one year, fifty percent of *TMPRSS-ERG+;Pb-Cre4+;Kras^{G12D/+}* mice (3 out of 6 mice) developed invasive adenocarcinoma with desmoplastic reaction in the stroma (Figure 1), while 5 out of 5 double transgenic mice showed no histological changes. IHC staining demonstrated that the tumor nests were strongly positive for KRT8 and negative for TP63, characteristic of luminal adenocarcinoma (Figure 1). These data are consistent with a *Kras^{G12V}* transgenesis model that demonstrated no changes or low-grade prostate intraepithelial neoplasia following *Pb-CRE* induction^{20, 21}.

Generation and characterization of prostate epithelial cell lines

To investigate the mechanism(s) accounting for the synergy between *TMPRSS2-ERG* and oncogenic RAS in promoting prostate tumor development, we sought to develop an in vitro system. Prostate luminal cell cultures historically have been difficult to establish from non-transformed primary prostate tissue, producing mixtures of mostly basal and intermediate cells. To promote the growth of luminal cells, we used culture conditions that modify tissue processing, culture substrate, and media components, originally developed to establish the growth of normal breast luminal epithelia and enrich for stem/progenitor cells

22. Cell lines were established from WT, *TMPRSS2-ERG* (T-E), and *Pb-CRE+;Tp53^{flox/flox}* prostates. Two independently established lines were characterized for each genotype. As shown in Fig. 2A, ERG was expressed at relatively similar levels in the *TMPRSS2-ERG* derived lines (labeled T-E-1 and T-E-2), and AR was expressed in all lines except T-E-1. Although *TMPRSS2* is AR-regulated, we previously have shown AR-independent driven-expression as well¹¹. RNA analyses confirmed the lack of *Tp53* in lines derived from *Pb-CRE+;Tp53^{flox/flox}* prostates (called p53^{pc-/-}-1 and -2) and also showed *Krt18* as highly expressed across all cultures (Fig. S1).

The WT and T-E lines were characterized for lineage heterogeneity across the populations using flow cytometry for quantification of intracellular KRT18 and KRT5. All cell lines were predominantly composed of KRT18 single positive cells, while there was some variability in the relative percentages of KRT5-/KRT18- double negative or KRT5+/KRT18+ double positive cells (Fig 2B). All populations exhibited a similar continuum in staining profiles with no unique subpopulations observed. The flow cytometry was validated by cytospin staining in T-E-2 cells for KRT8 and KRT5 where approximately 90% of cells stained positive for KRT8 only (Fig. 2C). Thus, luminal cells were the major cell type that established and proliferated under the selected conditions.

The quantification of sphere-forming units (SFU) in Matrigel is a measure of self-renewing stem/progenitor activity. Consistent with increased SFU observed in single cells processed directly from the *TMPRSS2-ERG* prostates¹¹, T-E-1 & T-E-2 contained substantially higher levels of multi-generation propagation activity than WT-1 cells (Fig. 2D). Consistent with this, a transcriptomic comparison of differentially expressed genes in T-E-1 compared to WT-1 shows a gene set enrichment of urogenital developmental genes, including *Tacstd2*, a marker of luminal stem cells²³, *Sox9*, and the developmentally regulated NOTCH pathway (Fig. 2E). NOTCH signaling²⁴ and *Sox9*²⁵ are previously identified ERG targets in prostate cancer cell lines.

Suppression of *Kras^{G12V}*-induced senescence by *TMPRSS2-ERG*

To analyze the interaction of the ERG and oncogenic RAS pathways, we infected the cell lines described above with lentivirus encoding constitutively expressed oncogenic *Kras^{G12V}*. Following selection for the presence of lentivirus, we observed over time extensive morphological senescence in WT-1 cells, but to a much lesser extent in T-E-1 and T-E-2 lines. After several weeks of culture, the remaining WT-1 cells that escaped senescence had been selected for low levels of RAS, while the T-E-1 and T-E-2 lines continued to grow and express elevated RAS and pERK (Fig. S2).

To investigate synchronized *Kras^{G12V}*-induced senescence, we developed a tetracycline regulated (tet-on) inducible system. Upon doxycycline induction, KRAS and downstream pERK were rapidly induced in all cell lines by day 2. However, similarly to constitutively expressed *Kras^{G12V}*, inducible *Kras^{G12V}(iKRAS)* levels and associated pERK were observed continuously in T-E-1 and T-E-2 cultures but were not maintained at day 9 in WT-1 cultures (Fig. 3A). We tested the growth kinetics of bulk WT-1, T-E-1, and T-E-2 lines following *Kras^{G12V}* induction (Fig. 3B). WT-1 iKRAS cells showed an inhibition in growth compared with no treatment, starting at day 5 after doxycycline induction and continuing

through the end of the assay at day 7. In contrast, *Kras*^{G12V} induction stimulated rather than hindered the growth in T-E-1 & T-E-2 iKRAS cell lines. These results further characterize the *Kras*^{G12V}-induced morphological growth arrest observed in non-transformed luminal cells and suggest that ERG may directly or indirectly influence this response.

To better compare the extent of the senescent response in WT vs. T-E cells, we quantified senescent clones following oncogenic *Ras* induction. Clonal colonies were allowed to develop, treated with doxycycline to induce *Kras*^{G12V} expression for 3 days and subsequently scored using staining for senescence-associated beta-galactosidase in combination with the presence of enlarged and flattened cells as phenotypic markers of senescence (Fig. 3C). Approximately 45% and 10% of WT-1 and T-E-1 iKRAS colonies, respectively demonstrated senescence, confirming the results from bulk cultures. To evaluate whether the suppression of oncogene-induced senescence was a direct effect of ERG, or alternatively, indirectly related to ERG influencing luminal cell development *in vivo*, we depleted *ERG* in T-E-1 cells using two independent lentivirus-mediated shRNA constructs and subsequently induced *Kras*^{G12V} in clonal colonies. As shown in Fig. 3C, shRNA mediated depletion of *ERG* increased iKRAS senescence approximately three-fold, suggesting an active role, at least in part, for ERG suppression of the observed senescent response.

Elevated TP53 expression following the induction of senescence has been described in a variety of models, including for mouse prostate carcinoma *in situ* (mPIN) lesions in progressive *Pten*^{-/-} prostate cancer models²⁶. Following oncogenic RAS induction, we did not observe robust TP53 increases in T-E lines, although there was small (approximately two-fold) increases in WT cells (Fig. 3A). To investigate the role of TP53 in a system of nontransformed prostate luminal cells, we introduced the tet-on *Kras*^{G12V} system into *Tp53* null p53^{Pc-/-}-1 cells and assessed senescent colonies following induction. As shown in Fig. 3C, *Tp53*^{-/-} luminal epithelial cells responded similarly as WT-1 cells with almost 50% senescent colonies, indicating that TP53 alone is not a major determinant of senescence induction to oncogenic RAS in luminal prostate cells.

As bulk cultures are more facile than clonal cultures, we sought a method to reliably quantify senescent cells in bulk culture. We developed an automated method based upon multiple morphological criteria using high-throughput confocal microscopy imaging (HTI). Two days after oncogenic RAS induction and prior to confluence, cells were stained with Cell Mask deep red and DAPI. After screening for more than 20 parameters, a machine learning algorithm identified individual parameters of cell number and cell area as quantitative measures of senescence, consistent with well-accepted characteristics. In addition, another parameter combined seven intracellular and nuclear characteristics to calculate the percentage of senescent cells (Fig. 4A, see Methods). Upon *Kras*^{G12V} induction, WT-1 and WT-2 iKras cells had significantly lower cell numbers compared to no treatment, while the cell numbers in T-E-1 and T-E-2 iKras changed minimally (Fig. 4A). Consistent with senescent morphologies, the average cell area in both WT-1 and WT-2 iKras cells significantly increased while the cell area remained the same in both T-E-1 and T-E-2 iKras cells (Fig. 4A). In WT-1 and WT-2 iKras cells, the percentage of senescent cells increased by 2- to 5-fold after *Kras* induction, consistent with colony assays, while there

was no change in T-E-1 and T-E-2 iKras cells (figure 4A). Similarly to the clonal analyses, p53^{Pc-/-}-1 and -2 cells demonstrated senescent characteristics upon *Kras*^{G12V} induction. It is likely that the relative percentage of senescent cells in p53^{Pc-/-} bulk culture is less than that in clonal cultures due to the overgrowth of TP53 null, non-senescent cells.

Senescent cells often express a senescence-associated secretory phenotype (SASP), which is composed of context determined chemokines, cytokines, growth factors, and small molecule metabolites²⁷. Among multiple candidate genes tested, IL-1 α is reported to be a master regulator in SASP and an effector of prostate cancer growth inhibition²⁷. We assayed RNA levels for IL-1 α and INHBA, a gene downstream of IL-1 α , in developed colonies after *Kras*^{G12V} induction. Both were substantially increased in WT-1 iKras cells while levels were more moderated in T-E-1 and T-E-2 iKras cells (Figure 4B). To determine whether IL-1 α influences prostate luminal cell growth in this system, different concentrations of neutralizing anti-IL-1 α antibody were added into the culture prior to *Kras*^{G12V} induction, and senescence parameters subsequently were quantified (Fig. S3). In addition, we added different concentrations of soluble IL-1 α into the cultures to evaluate whether high dose of IL-1 α is sufficient to induce senescence (Fig. S3). The patterns for cell numbers, cell area, and percentage of senescent cells with anti-IL-1 α or IL-1 α treatments did not change compared to corresponding control groups, suggesting that IL-1 α is a senescence marker but not a senescence effector in this model.

Over-expression of *ERG* in WT-1 iKras cells rendered the cells resistant to *Kras*^{G12V}-induced senescence

To further confirm that the expression of ERG accounts for the resistance to *Kras*^{G12V}-induced senescence, we infected WT-1 iKras cells with lentivirus generated from a human *ERG* (hERG) expression construct. The expression level of hERG in WT-1 iKras cells was low compared to endogenous level of TMPRSS2-ERG in T-E-1 cells (Figure 5A). However, even such low-level expression of hERG reversed WT-1 *Kras*^{G12V}-induced senescence (Figure 5B). In addition, the over-expression of hERG in WT-1 iKras cells also reversed the upregulation of IL-1 α upon *Kras*^{G12V} induction (Figure 5C).

TMPRSS2-ERG can bypass PTEN deletion-induced senescence

PTEN deletion is a common oncogenic event in primary prostate cancer. To evaluate whether the function of TMPRSS2-ERG in bypassing *Kras*^{G12V}-induced senescence can be generalized to other oncogenic events such as *PTEN* deletion, we depleted *Pten* in cells using tet-on inducible *Pten* shRNAs. In WT-1 and T-E-1 cells, *PTEN* depletion correlated with elevated levels of pAKT, as expected (Figure 6A). *PTEN* reduction in WT cells induced senescence, indicated by a 2-fold increase in IL-1 α mRNA and increased senescence parameters (Figure 6B&C). By comparison, upon *Pten* depletion, T-E-1 cells manifested no change in growth or IL-1 α mRNA levels and minor changes relative to WT-1 cells in morphological parameters (Figure 6B&C). These results suggest that TMPRSS2-ERG opposes senescence induced by partial *PTEN* loss. We note that TP53 appeared to be weakly induced in both WT-1 and T-E-1 cells following *PTEN* depletion, suggesting that differences in TP53 cannot account for senescence resistance.

TMPRSS2-ERG cells demonstrate increased MYC pathway activation relative to WT cells

We examined several downstream mediators of RAS-dependent senescence signaling. Following *Ras*^{G12V} induction, Phospho-ERK, a major mediator of RAS pathway activation, showed relatively equivalent levels and kinetics in WT, T-E, and TP53 null lines (Figure 7A), while modest AKT phosphorylation induction was observed only in *Tp53*^{-/-} cells (Figure 7B). Frequent markers of RAS-induced senescence, the CDK inhibitors *Cdkn1a* (p21) and *Cdkn2a* (p16), were not demonstrably increased in WT and T-E cell lines. By comparison, both were induced in TP53 null cells, suggesting that alternative signaling pathways associated with senescence are context-dependent and distinct for WT and TP53 null luminal prostate cells. It should be noted that although *Cdkn1a* is a TP53 target, several other modes of regulation have been described²⁸. Phospho-RB levels decreased in TP53 null cells at day 5, consistent with delayed kinetics relative to CDKN2A expression. Another recurring feature of RAS-induced senescence is increased DNA damage secondary to replicative stress^{17, 18, 29}. As shown in Figure 7C, although there was a statistically significant increase in γ H2AX staining following *Ras*^{G12V} induction in WT but not T-E cell lines, the absolute level of DNA damage was variable across senescence-susceptible and resistant cell lines, including a relatively low level of damage in WT-2 cells undergoing senescence, and a modest increase in DNA damage in WT cells of only ~30%. These data suggest that distinctions in the levels of DNA damage do not account for differences in senescence induction.

To analyze the effect of ERG on *Ras*^{G12V}-induced transcription, we performed a time course of gene expression at 0, 3, and 5 days after RAS induction in WT-1 and T-E-2 cells, both of which are AR⁺. To better understand the ability of ERG to modulate the response to induced RAS over the 5 day time period, two differential gene expression testing regimes were employed. First, a paired analysis identified genes differentially expressed after RAS induction that were consistent between the wild type and transgenic models. These are genes that are induced by RAS independent of ERG. Second, an interaction effect analysis identified genes differentially expressed over time in response to RAS induction that were modulated by the presence of ERG. Significantly differentially expressed genes detected under both regimes (i.e the intersecting set in Figure 8A) represent genes whose response to RAS is in the same direction over time but amplified by the presence of ERG. As shown in Figure 8A, ~80% of the DEGs demonstrated paired expression at day 3, showing predominantly similar initial responses to oncogenic RAS induction in WT and ERG-expressing cell lines. The transcriptional patterns between WT-1 and T-E-2 became more discordant at day 5, as shown by a proportional increase in genes demonstrating an interaction expression pattern, and consistent with different fates of the cell lines.

To determine the major pathways that were activated upon *Ras*^{G12V} induction, we applied GSEA analysis to DEGs in each model at days 3 and 5. To identify significant divergence in the transcriptomic responses between WT and T-E lines, we analyzed the relative difference in the models over time (TE/WT). Figure 8B is a dot plot summary of enrichment scores for such analyses showing a number of RAS responsive pathways. Consistent with the paired analysis described above, RAS targets (KRAS lung breast up V1 up) increased in both WT and T-E cells at day 3 but dropped off in WT cells at day 5. One differential

response, translational elongation (Reactome eukaryotic translation elongation), increased slightly in T-E-2 while decreasing dramatically at day 3 upon *Ras*^{G12V} induction in WT cells (Fig. 8B). Several genes in the translational elongation pathway are contained within “MYC targets,”^{30,31} (Hallmark MYC target V1) and this broader category demonstrated an overall similar differential kinetic response. As shown in Figure 7B, MYC protein was not notably changed upon *Ras*^{G12V} expression, although baseline MYC levels were higher in those lines expressing ERG, consistent with previous reports that MYC is positively regulated by ERG⁸. Another RAS-responsive pathway, SREBP-regulated cholesterol synthesis³⁰ (Reactome cholesterol biosynthesis) decreased significantly at day 5 in WT-1 cells, while maintaining stable levels of expression in ERG expressing cells. Other pathways that were differentially increased in T-E-2 cells were chemokines and their receptors (Reactome chemokine receptors bind chemokines) and angiogenesis (Hallmark angiogenesis), while by contrast, IFN targets (Heckner IFNB1 targets) were more robustly expressed in WT-1 cells. E2F regulated replication genes (Replication cluster) decreased after *Ras*^{G12V} induction in both models³¹, although significantly greater in WT-1 than T-E-2 cells. Because time 0 cells were exponentially growing, the decrease seen in T-E-2 cells with time, despite increased cell numbers, may have been the result of the relatively small numbers of cells (Figs. 3 and 4) that undergo senescence. In summary, T-E cells increased or maintained growth promoting pathways in response to oncogenic RAS while WT cells inactivated anabolic responses such as translation and lipid synthesis.

Protein translation and SREBP mediated lipid synthesis are regulated by mTORC1 signaling^{32,33}. To investigate the role mTORC1 in senescence resistance of ERG-expressing cells, we analyzed the effect of inhibiting the mTORC and MEK/ERK pathways on *Ras*^{G12V}-induced senescence in WT-1 and T-E-1/2 cells. As shown in Figure 8C, mTORC inhibition induced a small amount (~10%) of senescence in WT cells and had an additive effect with *Ras*^{G12V} induction. mTORC inhibition alone in T-E cell lines had little effect, but importantly, interfered with senescence resistance normally seen after *Ras*^{G12V} induction. By comparison, MEK/ERK inhibition induced senescence equivalently in WT-1 and T-E lines and suppressed additional *Ras*^{G12V} mediated senescence in WT-1 cells. Taken together these analyses implicate mTORC as a component of ERG-mediated senescence resistance and in addition, demonstrate that T-E cells are competent to undergo senescence.

TMPRSS2-ERG and constitutively active *Kras*^{G12V} synergize to promote prostate tumorigenesis and metastasis.

To analyze the tumorigenic potential of the TMPRSS2-ERG expressing cell lines, we infected WT-1, T-E-1 and T-E-2 cells with Luc-GFP lentiviruses followed by constitutively active *Kras*^{G12V} lentiviruses. As described earlier (Fig S2), WT-1 *Kras*^{G12V} cells, underwent widespread senescence and the resistant cells that emerged had lower levels of KRAS and pERK expression as compared to *Kras*^{G12V} infected T-E-1 and T-E-2 lines.

We performed orthotopic injection of four groups (WT-1 luc-GFP control, WT-1 luc-GFP *Kras*^{G12V}, T-E-2 luc-GFP control, T-E-2 luc-GFP *Kras*^{G12V}). Monitoring by bioluminescent imaging showed no demonstrable growth in the first three groups up to 6 months after injection. In contrast, 14 out of 16 nude mice injected with T-E-2 luc-GFP *Kras*^{G12V}

developed orthotopic tumors within 3 weeks (Supplementary Table 1 and Fig. S4A), which subsequently showed metastatic spread. Histological analysis demonstrated a mesenchymal carcinoma histology, elongated spindle-shaped cells positive for pan cytokeratin staining, pERK, and sporadic ERG expression (Fig. S4A). These results are consistent with the phenotypic characteristics of other models of oncogenic RAS transformed mouse prostate cancer models^{34, 35}.

Metastatic potential was further analyzed following intracardiac injection of the above four models. None of the three control groups metastasized up to six months after injection (Supplementary table 1). In contrast, bioluminescent imaging showed wide-spread metastatic colonization in mice injected with T-E-2 luc-GFP *Kras*^{G12V} cells (Supplementary table 1). The most common sites of metastasis were long bones (9 out of 16 mice), testicles/epididymis area (5/16), and brain (3/16) (Supplementary figure S4B&C). In conclusion, *TMPRSS2*-*ERG* expressing prostate luminal cells, which maintain oncogenic RAS expression, display high tumorigenic and metastatic potential.

Discussion:

ERG translocations are considered to be one of the initiating genomic events in prostate cancer, based upon their prevalence and their presence in the earliest pathologically defined neoplastic lesions^{1, 2}. Translocations lead to *ERG* expression, which is normally silent in prostate epithelia. We present data supporting the concept that *ERG* primes prostate epithelial cells for subsequent genomic events by opposing oncogene induced senescence, rationalizing the early occurrence and order of accumulating mutations. In an FVB transgenic mouse model, *TMPRSS2* promoter driven *ERG* expression accelerated the early development but not the progression of *Pten*^{+/-} lesions^{11, 14}. In addition, as shown here, *ERG* expression was necessary for oncogenic *Kras* initiated prostate adenocarcinoma. In luminal cell lines derived from wild type or transgenic mice, *TMPRSS2*-*ERG* opposed *Kras*^{G12V} or *Pten* loss induced senescence to promote *Kras*^{G12V}-dependent tumorigenicity and metastasis. Phenotypic characteristics associated with *ERG* expression in nontransformed cells such as increased self-renewal and *MYC* expression pose the interesting possibility that there is an underlying link between the mechanisms influencing stemness and resistance to senescence.

Why has senescence resistance not been previously appreciated as a function of *ERG*? The ability to investigate preneoplastic activity depends upon the availability of relevant cancer cells of origin, either in the form of in vitro cell models or identifiable tumor-initiating cells in transgenic mouse models. Studies have not been performed with non-viral immortalized, prostate luminal cultures due to the challenges of establishing and growing such cells. Cell line models such as VCaP, PC3, and RWPE previously used to analyze *ERG* function are not expected to be susceptible to senescence induction since they were derived from prostate cancer metastases or HPV-immortalized epithelium, which disrupts cell cycle regulation. Using methods adapted for culturing mammary luminal stem cells²², we produced prostate luminal cell lines from wild type (i.e. normal), a BAC-encoded *TMPRSS2*-driven *ERG* (T-E) transgenic model, and *Tp53* null adult prostates. By comparing the consequences of *ERG* presence and absence following oncogenic activation, we have observed *ERG* dependent

senescence resistance. Importantly, depletion of *ERG* in T-E cells led to increased oncogene induced senescence, while ectopic *ERG* expression in WT cells reduced senescence induction (Figures 3C and 5). Using parallel methodology for cell line establishment, Zhang et al. have described human prostate luminal progenitor cell cultures sensitive to transformation by *ERG/AKT/AR*³⁶. However, because the oncogenes were introduced simultaneously and subsequently selected in vivo, the experimental protocol did not lend itself to the observation of senescence.

Various cell lineage and context dependence mechanisms have been shown to influence senescence induction and resistance. The classical oncogene-induced senescent pathways of RB1 inhibition and TP53 induction are common effectors of growth inhibition in many examples of senescence³⁶. However, the induction of cell cycle inhibitors CDKN2B (p16), CDKN1A (p21), or TP53 were not readily observed at the protein or transcriptional level in senescent WT prostate luminal cells. DNA damage coupled to replication stress is an inducer of senescence in many models of RAS-mediated OIS^{17, 29}, although there was no correlation between γ H2AX levels and senescence in the cell lines used here (Fig. 7C). Instead, WT OIS was evident as morphological transformation and growth inhibition. By contrast, cell lines derived from TMPRSS2-ERG prostates showed substantially reduced OIS responses as determined by their continued growth and by clonal and bulk population single cell imaging analyses (Figs. 3B&C and 4). Consistent with the lack of TP53 protein induction in senescent WT cells, we observed a robust senescence response following *Ras*^{G12V} induction in polyclonal TP53 null lines, clearly demonstrating that senescence of normal luminal prostate epithelia occurs in the absence of TP53. The senescence response of WT and TP53 null cells was distinct, with the latter demonstrating obvious CDKN2B and CDKN1A induction, possibly reflecting changes to the regulation of senescence signaling circuitry following *Tp53* loss. It should be noted that previous studies describing *Tp53*-dependent senescence in *Pten* null prostates evaluated progression from neoplastic lesions²⁶, not initiation from normal luminal cells as was done here.

Importantly, early signal transduction in WT and T-E cells following *Kras*^{G12V} induction appeared similar, suggesting equivalent signal initiation in the different cell lines. For example, ERK phosphorylation kinetics were equivalent, and there was an 80% overlap in induced transcriptional responses at day 3. Compared to WT, the transcriptional pathways in TMPRSS2-ERG cells that diverged included a relative increase in MYC targets, ribosome biogenesis, protein translation, and lipogenesis. MYC, a known ERG target⁸, demonstrated higher baseline expression in T-E relative to WT lines (Fig. 7B). Importantly, higher MYC levels are observed in *ERG* positive compared to *ERG* negative clinical samples, independent of MYC gene amplification¹⁴. MYC influences the transcription of several genes within the differentially expressed pathways increased in T-E cells^{30,31}. mTOR inhibitors, whose physiological targets include protein translation and lipogenesis pathways^{32, 33}, reversed senescence resistance in T-E cells but had relatively little effect on overall senescence levels in WT cells (Fig. 8C), supporting the functional significance of these differentially expressed pathways. MYC suppresses OIS in a variety of cancer models³⁷, most likely through pleiotropic effects on a network of genes influencing growth and differentiation. We also note that in various systems and models, including prostate, MYC

represses terminal differentiation and promotes stem cell functions such as self-renewal^{38, 39}, consistent with the phenotype described for the *TMPRSS2-ERG* model.

Given the high frequency of *TMPRSS2-ERG* fusions in clinical prostate cancer and its potential role in oncogenic initiation, the biological functions of *TMPRSS2-ERG* are of significant interest. Our study demonstrates that by suppressing oncogenic RAS- or *Pten* depletion-induced senescence, *TMPRSS2-ERG* conditions transformation in pre-malignant cells. Because prior studies have not been designed to address the concept of ERG-dependent senescence resistance, our data provide a basis for further contextual and mechanistic studies to more fully address ERG functions in prostate cancer. Future histopathological studies in either human tissue or mouse models will require the development of in vivo senescence markers observable in premalignant tissues.

Materials and Methods:

In vivo animal model

TMPRSS2-ERG A5 transgenic mice were generated and characterized as described¹¹. *PB-Cre4⁺* mice (strain#01XF5) and LSL *Kras* G12D (strain#01XJ6) mice were obtained from the Mouse Models of Human Cancers Consortium Mouse Repository (Frederick, MD). *TMPRSS2-ERG⁺*; *Kras*^{G12D/+}; *PB-Cre4⁺* triple transgenic mice, *Kras*^{G12D/+}; *PB-Cre4⁺* double transgenic mice were produced by breeding 8- to 10-week-old *TMPRSS2-ERG⁺*; *Kras*^{G12D/+} females with *PB-Cre4⁺* males. Animals were bred, housed, and used in accordance with the Policy on Humane Care and Use of Laboratory Animals (Office of Laboratory Animal Welfare, National Institutes of Health, Bethesda, MD). Histological analyses were performed by a pathologist on a blind fashion.

Generation of prostate epithelial cell lines from WT, *TMPRSS2-ERG* transgenic, and *Tp53^{fl/fl}*; *PB-Cre4* mice:

To generate murine prostate epithelial cell lines from tumor-free normal prostate tissues, the entire urogenital tract was isolated and prostate lobes were dissected out, minced, and digested for 1 hour at 37°C with rotation in DMEM medium containing Collagenase IV (1mg/ml; Roche) and DNase I (1mg/ml; Sigma). The resulting organoids were washed once with PBS, resuspended in WIT-P medium²², (Cellaria), passed five times through a 19g needle, plated into six-well Primaria plates (BD Biosciences) and passaged every 7 days for at least four passages before characterization. The establishment rate was ~10%, except for TP53 null genotypes, which were established at 100% frequency.

Real-time qPCR:

Total RNA was extracted from samples with a RNeasy Mini Kit (Qiagen). 500ng of total RNA was converted to cDNA using a SuperScript III first-strand synthesis system kit (Life Technologies). qPCR was performed with the FastStart Universal SYBR Green Master Mix (Roche) on a StepOnePlus Real-Time PCR machine (Applied Biosystems). Data were normalized to GAPDH using the 2^{-Ct} method.

Protein extraction and Western blot analysis:

All lysates were prepared using RIPA buffer containing phosphatase inhibitor (Bimake, Houston, TX) and protease inhibitor (Roche). Western blots were performed on 4-20% Tris Glycine gels (Bio-Rad), transferred to PVDF membranes, and blocked in 5% dry milk in PBST at room temperature for 1 hour. Primary antibodies were incubated overnight at 4°C and secondary antibodies (Fisher Scientific) were incubated for 1 hour at room temperature at 1:2000 dilution. Western blots were exposed using Clarity Western ECL Substrate (Bio-Rad) or Super Signal Femto Maximum Sensitivity Substrate (Thermo Fisher) on a ChemiDoc Touch exposure system (Bio-Rad).

Intracellular staining of KRT5 and KRT18 and flow cytometry analysis:

Cells were fixed in formaldehyde-based fixation buffer (Santa Cruz) at 1×10^6 cells/ml at 4°C for 20 min, washed once in saponin containing Perm/Wash buffer (BD Biosciences, RRID:SCR_013311), incubated at 4°C for 10 min with Fc blocker at $1 \mu\text{g}/10^6$ cells (BD Biosciences), incubated at 4°C for 30 min with primary FITC-KRT18 (Abcam; catalogue #ab52459) and unconjugated rabbit anti-KRT5 (BioLegend cat#905501) antibodies at $1 \mu\text{g}/10^6$ cells. Cells were washed once in Perm/Wash buffer, followed by incubating at 4°C for 30 min with secondary Alexa647 goat anti-rabbit IgG F(ab')₂ antibody (Life Technologies; catalogue#A-21246) at 1:250 dilution. Cells were washed in PBS and run on a FACS Calibur with matching isotype control antibodies: FITC-mouse IgG1 (Abcam; catalogue #18435) and rabbit IgG (Life Technologies; catalogue #02-6102) as the negative controls for gating. Analysis was performed using FlowJo (FlowJo, RRID:SCR_008520), and all experiments were repeated a minimum of three times.

Cytospin staining

Single-cell suspensions were washed twice with PBS, and 1×10^4 cells were deposited on glass slides in PBS by centrifugation at 1,000 rpm for 2 min using a cytospin system from Thermo Shandon. Cells were fixed, permeabilized, blocked and stained with primary KRT5 and KRT8 antibodies (BioLegend) followed by Alexa-488 and -568 conjugated secondary antibodies as described⁴⁰. To quantify cytokeratin staining, at least 300 cells were manually counted using a 63x objective of the upright fluorescent Zeiss Axioplan microscope.

Genetically engineered cell lines

Genetically modified cell lines were established using lentiviral vectors following standard procedures. All lentiviral vectors were constructed by the Protein Expression Laboratory, National Cancer Institute. Constitutively-active human *KRAS*^{G12V} was expressed from the β -actin CAG promoter. For expression of tet-on inducible gene(s), including *KRAS*^{G12V} and *Pten* shRNA, cells were first selected for infection with Tet-On 3G transactivator lentiviruses, followed by selection for the target gene of interest under the control of the TRE3G promoter. For ectopic expression of *ERG*, cells were selected for infection with pFUGW lentiviruses encoding human *ERG* expressed from the EF1 α promoter.

***In vivo* prostate tumorigenesis and metastasis assay**

In vivo orthotopic injections for tumorigenesis or intracardiac injections for metastasis were performed as previously described⁴¹ using 6- to 7-week-old athymic nude mice (Ncr *nu/nu*) and 1×10^6 cells/mouse from WT luc-GFP control, WT luc-GFP KRAS^{G12V}, TMPRSS2-ERG luc-GFP control, or TMPRSS2-ERG luc-GFP KRAS^{G12V} cell lines. Tumor development was monitored weekly starting 3 weeks after injection by bioluminescent imaging, which were acquired with an IVIS imaging system (Xenogen) as previously described⁴². For each group, 3-5 mice were inoculated. The number of mice for each experiment was determined based on preliminary experiment to ensure the potential to reach $p < 0.05$ with a power of 80%. Mice were allocated in each group by simple randomization. No mice were excluded from the analysis. Tumor cell inoculation and imaging were performed by two different researchers on a blind fashion.

Histology and Immunohistochemistry:

Immunohistochemistry was performed as described previously⁴³. Bones were decalcified in 10% EDTA for 2 weeks before processing. Tumors or prostate tissues were fixed in 4% PFA, transferred to 70% ethanol, and trimmed before standard histological processing, sectioning, and H&E staining performed by Histoserv Inc. (Germantown, MD). H&E and IHC slides were scanned using a Carl Zeiss AxioScan Z1 microscope with a 20X/NA 0.8 plan apochromat objective (Zeiss, Germany). The scale bars in the figures indicated the power of magnification at which the images were captured from the virtual microscope slides.

2D clonal culture, 3D Sphere forming assay and propagation of spheres

To evaluate cellular proliferation, soluble factors secreted by senescent cells and proteins involved in senescent pathways, we performed assays on clonally cultured cells. Single cell suspensions were generated from trypsinized cells by sequentially passing through 22-, 23-, 25-, 27-, and 30-gauge needles to break up small cell clumps. The resultant suspension was counted, and 4000 cells were plated into a 10cm² dish. Single cells were grown for 6-8 days to allow the formation of small colonies prior to no further treatment or treatment with 1 μ g/ml doxycycline to induce *Kras*^{G12V} expression. Cells were harvested at different time points as indicated in the figures and processed for protein or total RNA extraction.

For sphere forming assays, single cells were prepared as described above. 2500 cells/well were mixed with Matrigel (BD) at 1:1 volume ratio and plated along the rim of a 12-well plate. Matrigel was allowed to solidify for 1 hr at 37°C in a humidified incubator before culture media were added. Media were changed every 2-3 days, and the number of spheres was counted at day 10 and calculated as the percentage of total number of cells plated. Propagation of spheres were performed as described¹¹. Spheres were serially passaged by harvesting, processing into single cells, and plating cells with Matrigel as described as above. G1 indicates the first generation of spheres derived from the cell lines. G2-G4 referred to as the subsequent generations of the serially passaged spheres.

Proliferation assay

Cell lines were processed to single cells as described above. Single cells were seeded in 96 well plates at 500 cells/well, incubated overnight and subsequently left untreated or treated with 1 μ g/ml doxycycline. The assay was terminated at different time points with MTS according to the manufacturer instructions (Promega) and read on a plate reader at 490nm absorbance. Assays were performed in triplicate and each cell line was repeated a minimum of three times. Background absorbance was removed before plotting the data and analyzing statistically using GraphPad Prism 8 software.

Senescence associated β -galactosidase cell staining and quantification

To measure senescence associated β -galactosidase, clonal cultures as described were established in 6-well plates at 500 cells/well. After small colonies formed from single cells, colonies were left untreated or treated for 3 days with 1 μ g/ml doxycycline to induce Kras^{G12V} expression. Colonies were washed, fixed and stained for senescence associated β -galactosidase (pH 6.0) according to the manufacturer's protocol (Cell Signaling; catalogue #9860). Senescent colonies were quantified based on the presence of beta-gal positive cells, which were usually heterogeneous within a colony, in combination with enlarged and flattened cell morphology.

γ H2AX and senescence quantification by Opera high-throughput fluorescence microscopy imaging:

For γ H2AX staining, cells were plated in optically clear bottomed CellCarrier96-well collagen coated plates (Perkin Elmer) and Kras^{G12V} was induced as described above. Fixed and permeabilized cells were incubated for 2 hours at room temperature with anti-phospho-histone H2A.X primary antibody (Millipore; catalogue #05-636) at 1:1000 dilution in PBS containing 2% goat serum and 2% BSA, followed by incubating with Alexa Fluor 568 anti-mouse secondary antibody at 1:200 dilution for 2 hours at room temperature in the dark. Finally, cells were stained with 0.13 μ g/ml of DAPI at room temperature for 2 minutes, washed and stored in PBS at 4°C before scanning.

For morphological determinations, cells were plated and induced as described above. Cells were washed in PBS three times between each treatment outlined below. Cells were fixed in 4% PFA at room temperature for 20 minutes, permeabilized with 1% Triton-X100 at room temperature for 10 minutes, followed by staining with HCS CellMask Deep Red (Invitrogen; catalogue #H32721) at 1:10,000 dilution to delineate the entire cells. Finally, cells were stained with 0.13 μ g/ml of DAPI at room temperature for 2 minutes, washed and stored in PBS at 4°C before scanning.

To develop HTI parameter, plates were scanned on PerkinElmer Opera QEHS, an automated, confocal high-throughput microscope. Data were processed on PerkinElmer Columbus, an image storage and analysis server. Pilot experiments were first performed to determine the optimal cell density, DAPI concentration, and HCS CellMask Deep Red concentration. Thirty-seven preset parameters in the Columbus software were analyzed on individual cells for the association with senescent phenotypes, which identified cell numbers and cell area as significant independent variables. To analyze cell numbers and

cell area, 30 randomly selected fields in each well were assessed. In addition, through the Columbus machine learning software, an additional compound parameter that combined seven intracellular and nuclear parameters (called “senescent cells”) was determined to distinguish between normal cells and senescent cells. Those parameters included cell width, cell ratio: width to length, cell area, cell roundness, nucleus symmetry, nucleus length, and nucleus radial relative deviation. For machine learning purposes, manually selected normal and senescent (flattened and enlarged) appearing cells were labeled and analyzed via the Columbus machine learning software to determine the best combinations of parameters to distinguish between the two groups of cells. General principle and applications of high-throughput imaging and imaging-based profiling can be found in this review article ⁴⁴.

Transcriptomic Analysis

Clonally cultured WT-1 iKras and T-E-2 iKras cells were plated in 10cm² dishes at 4000 cells/dish in triplicate for each time point. After small colonies were established at day 6, 1µg/ml of doxycycline was added to induce Kras^{G12V} expression for 3 or 5 days. Cells were directly lysed on the dish with RLT buffer in RNeasy Mini Kit (Qiagen) and total RNA was extracted according to manufacturer’s protocol (Qiagen). Sequencing was performed by the CCR Sequencing Facility at National Cancer Institute.

Reads were aligned using the nextflow core RNA seq pipeline version 1.4.2 as described in ⁴⁵. Briefly reads were trimmed and aligned to hg19 using STAR (STAR, RRID:SCR_004463), and reads were quantified using featureCounts (featureCounts, RRID:SCR_012919). Differential expression analysis was performed using the edgeR (edgeR, RRID:SCR_012802) R package library. Counts were normalized using TMM normalization, and differences between conditions were tested using the quasiliikelihood framework ⁴⁶. To assess differences between conditions and over time, a two-way test was applied, and one-way tests were used to assess differences between conditions at each time point and differences within conditions across time points. Gene set enrichment analysis was performed using the clusterProfiler (clusterProfiler, RRID:SCR_016884) package⁴⁷ with the gene sets available in the msigdb package. Each collection underwent GSEA testing independently.

Statistics

All statistical analyses were performed using GraphPad Prism 8 (GraphPad Prism, RRID:SCR_002798) with unpaired two-tailed student *t* test. *P* value > 0.05 is not considered statistically significant. Single asterisk (*) indicates *p* < 0.05, double asterisks (**) indicate *p* < 0.01, triple asterisks (***) indicate *p* < 0.001, quadruple asterisks (****) indicate *p* < 0.0001. Error bars represent ± SEM. GraphPad Prizm performed an F test to compare variances, and the variances were similar between the groups that are being statistically compared.

Supplementary Material

Refer to Web version on PubMed Central for supplementary material.

Acknowledgement

We thank Dr. Gianluca Pegoraro and Laurent Ozburn for their assistance at setting up and running Opera high throughput confocal imaging experiments and Neil Alilin for his assistance at managing mouse colonies and in vivo imaging.

This work was funded by the Intramural Research Program, National Institutes of Health, National Cancer Institute, Center for Cancer Research.

Data availability statement

RNAseq datasets generated and analyzed during the current study is deposited into BioProject database with ID: PRJNA801601

References

1. Cancer Genome Atlas Research N. The Molecular Taxonomy of Primary Prostate Cancer. *Cell* 2015; 163(4): 1011–25. [PubMed: 26544944]
2. Arora K, Barbieri CE. Molecular Subtypes of Prostate Cancer. *Curr Oncol Rep* 2018; 20(8): 58. [PubMed: 29858674]
3. Furusato B, Gao CL, Ravindranath L, Chen Y, Cullen J, McLeod DG et al. Mapping of TMPRSS2-ERG fusions in the context of multi-focal prostate cancer. *Mod Pathol* 2008; 21(2): 67–75. [PubMed: 18065961]
4. Birdsey GM, Shah AV, Dufton N, Reynolds LE, Osuna Almagro L, Yang Y et al. The endothelial transcription factor ERG promotes vascular stability and growth through Wnt/beta-catenin signaling. *Dev Cell* 2015; 32(1): 82–96. [PubMed: 25584796]
5. Knudsen KJ, Rehn M, Hasemann MS, Rapin N, Bagger FO, Ohlsson E et al. ERG promotes the maintenance of hematopoietic stem cells by restricting their differentiation. *Genes Dev* 2015; 29(18): 1915–29. [PubMed: 26385962]
6. Nicholas TR, Strittmatter BG, Hollenhorst PC. Oncogenic ETS Factors in Prostate Cancer. *Adv Exp Med Biol* 2019; 1210: 409–436. [PubMed: 31900919]
7. Sandoval GJ, Pulice JL, Pakula H, Schenone M, Takeda DY, Pop M et al. Binding of TMPRSS2-ERG to BAF Chromatin Remodeling Complexes Mediates Prostate Oncogenesis. *Mol Cell* 2018; 71(4): 554–566 e7. [PubMed: 30078722]
8. Sun C, Dobi A, Mohamed A, Li H, Thangapazham RL, Furusato B et al. TMPRSS2-ERG fusion, a common genomic alteration in prostate cancer activates C-MYC and abrogates prostate epithelial differentiation. *Oncogene* 2008; 27(40): 5348–53. [PubMed: 18542058]
9. Tomlins SA, Laxman B, Varambally S, Cao X, Yu J, Helgeson BE et al. Role of the TMPRSS2-ERG gene fusion in prostate cancer. *Neoplasia* 2008; 10(2): 177–88. [PubMed: 18283340]
10. Hollenhorst PC, Ferris MW, Hull MA, Chae H, Kim S, Graves BJ. Oncogenic ETS proteins mimic activated RAS/MAPK signaling in prostate cells. *Genes Dev* 2011; 25(20): 2147–57. [PubMed: 22012618]
11. Casey OM, Fang L, Hynes PG, Abou-Kheir WG, Martin PL, Tillman HS et al. TMPRSS2- driven ERG expression in vivo increases self-renewal and maintains expression in a castration resistant subpopulation. *PLoS One* 2012; 7(7): e41668. [PubMed: 22860005]
12. Li F, Yuan Q, Di W, Xia X, Liu Z, Mao N et al. ERG orchestrates chromatin interactions to drive prostate cell fate reprogramming. *J Clin Invest* 2020; 130(11): 5924–5941. [PubMed: 32701507]
13. Carver BS, Tran J, Gopalan A, Chen Z, Shaikh S, Carracedo A et al. Aberrant ERG expression cooperates with loss of PTEN to promote cancer progression in the prostate. *Nat Genet* 2009; 41(5): 619–24. [PubMed: 19396168]
14. King JC, Xu J, Wongvipat J, Hieronymus H, Carver BS, Leung DH et al. Cooperativity of TMPRSS2-ERG with PI3-kinase pathway activation in prostate oncogenesis. *Nat Genet* 2009; 41(5): 524–6. [PubMed: 19396167]

15. Mounir Z, Lin F, Lin VG, Korn JM, Yu Y, Valdez R et al. TMPRSS2:ERG blocks neuroendocrine and luminal cell differentiation to maintain prostate cancer proliferation. *Oncogene* 2015; 34(29): 3815–25. [PubMed: 25263440]
16. Chen Y, Chi P, Rockowitz S, Iaquina PJ, Shamu T, Shukla S et al. ETS factors reprogram the androgen receptor cistrome and prime prostate tumorigenesis in response to PTEN loss. *Nat Med* 2013; 19(8): 1023–9. [PubMed: 23817021]
17. Herranz N, Gil J. Mechanisms and functions of cellular senescence. *J Clin Invest* 2018; 128(4): 1238–1246. [PubMed: 29608137]
18. Zhu H, Blake S, Kusuma FK, Pearson RB, Kang J, Chan KT. Oncogene-induced senescence: From biology to therapy. *Mech Ageing Dev* 2020; 187: 111229. [PubMed: 32171687]
19. He S, Sharpless NE. Senescence in Health and Disease. *Cell* 2017; 169(6): 1000–1011. [PubMed: 28575665]
20. Pearson HB, Pesse TJ, Clarke AR. K-ras and Wnt signaling synergize to accelerate prostate tumorigenesis in the mouse. *Cancer Res* 2009; 69(1): 94–101. [PubMed: 19117991]
21. Scherl A, Li JF, Cardiff RD, Schreiber-Agus N. Prostatic intraepithelial neoplasia and intestinal metaplasia in prostates of probasin-RAS transgenic mice. *Prostate* 2004; 59(4): 448–59. [PubMed: 15065094]
22. Ince TA, Richardson AL, Bell GW, Saitoh M, Godar S, Karnoub AE et al. Transformation of different human breast epithelial cell types leads to distinct tumor phenotypes. *Cancer Cell* 2007; 12(2): 160–70. [PubMed: 17692807]
23. Karthaus WR, Hofree M, Choi D, Linton EL, Turkecul M, Bejnood A et al. Regenerative potential of prostate luminal cells revealed by single-cell analysis. *Science* 2020; 368(6490): 497–505. [PubMed: 32355025]
24. Kron KJ, Murison A, Zhou S, Huang V, Yamaguchi TN, Shiah YJ et al. TMPRSS2-ERG fusion co-opts master transcription factors and activates NOTCH signaling in primary prostate cancer. *Nat Genet* 2017; 49(9): 1336–1345. [PubMed: 28783165]
25. Cai C, Wang H, He HH, Chen S, He L, Ma F et al. ERG induces androgen receptor-mediated regulation of SOX9 in prostate cancer. *J Clin Invest* 2013; 123(3): 1109–22. [PubMed: 23426182]
26. Chen Z, Trotman LC, Shaffer D, Lin HK, Dotan ZA, Niki M et al. Crucial role of p53-dependent cellular senescence in suppression of Pten-deficient tumorigenesis. *Nature* 2005; 436(7051): 725–30. [PubMed: 16079851]
27. Faget DV, Ren Q, Stewart SA. Unmasking senescence: context-dependent effects of SASP in cancer. *Nat Rev Cancer* 2019; 19(8): 439–453. [PubMed: 31235879]
28. El-Deiry WS. p21(WAF1) Mediates Cell-Cycle Inhibition, Relevant to Cancer Suppression and Therapy. *Cancer Res* 2016; 76(18): 5189–91. [PubMed: 27635040]
29. Dimauro T, David G. Ras-induced senescence and its physiological relevance in cancer. *Curr Cancer Drug Targets* 2010; 10(8): 869–76. [PubMed: 20718709]
30. Ricoult SJ, Yecies JL, Ben-Sahra I, Manning BD. Oncogenic PI3K and K-Ras stimulate de novo lipid synthesis through mTORC1 and SREBP. *Oncogene* 2016; 35(10): 1250–60. [PubMed: 26028026]
31. Chicas A, Wang X, Zhang C, McCurrach M, Zhao Z, Mert O et al. Dissecting the unique role of the retinoblastoma tumor suppressor during cellular senescence. *Cancer Cell* 2010; 17(4): 376–87. [PubMed: 20385362]
32. Liu GY, Sabatini DM. mTOR at the nexus of nutrition, growth, ageing and disease. *Nat Rev Mol Cell Biol* 2020; 21(4): 183–203. [PubMed: 31937935]
33. Peterson TR, Sengupta SS, Harris TE, Carmack AE, Kang SA, Balderas E et al. mTOR complex 1 regulates lipin 1 localization to control the SREBP pathway. *Cell* 2011; 146(3): 408–20. [PubMed: 21816276]
34. Arriaga JM, Panja S, Alshalalfa M, Zhao J, Zou M, Giacobbe A et al. A MYC and RAS co-activation signature in localized prostate cancer drives bone metastasis and castration resistance. *Nat Cancer* 2020; 1(11): 1082–1096. [PubMed: 34085047]
35. Mulholland DJ, Kobayashi N, Ruscetti M, Zhi A, Tran LM, Huang J et al. Pten loss and RAS/MAPK activation cooperate to promote EMT and metastasis initiated from prostate cancer stem/progenitor cells. *Cancer Res* 2012; 72(7): 1878–89. [PubMed: 22350410]

36. Zhang D, Lin K, Lu Y, Rycaj K, Zhong Y, Chao HP et al. Developing a Novel Two-Dimensional Culture System to Enrich Human Prostate Luminal Progenitors that Can Function as a Cell of Origin for Prostate Cancer. *Stem Cells Transl Med* 2017; 6(3): 748–760. [PubMed: 28297567]
37. Wu CH, van Riggelen J, Yetil A, Fan AC, Bachireddy P, Felsher DW. Cellular senescence is an important mechanism of tumor regression upon c-Myc inactivation. *Proc Natl Acad Sci U S A* 2007; 104(32): 13028–33. [PubMed: 17664422]
38. Civenni G, Malek A, Albino D, Garcia-Escudero R, Napoli S, Di Marco S et al. RNAi-mediated silencing of Myc transcription inhibits stem-like cell maintenance and tumorigenicity in prostate cancer. *Cancer Res* 2013; 73(22): 6816–27. [PubMed: 24063893]
39. Lin CH, Lin C, Tanaka H, Fero ML, Eisenman RN. Gene regulation and epigenetic remodeling in murine embryonic stem cells by c-Myc. *PLoS One* 2009; 4(11): e7839. [PubMed: 19915707]
40. Abou-Kheir WG, Hynes PG, Martin PL, Pierce R, Kelly K. Characterizing the contribution of stem/progenitor cells to tumorigenesis in the Pten^{-/-}TP53^{-/-} prostate cancer model. *Stem Cells* 2010; 28(12): 2129–40. [PubMed: 20936707]
41. Yin J, Pollock C, Tracy K, Chock M, Martin P, Oberst M et al. Activation of the RalGEF/Ral pathway promotes prostate cancer metastasis to bone. *Mol Cell Biol* 2007; 27(21): 7538–50. [PubMed: 17709381]
42. JuanYin J, Tracy K, Zhang L, Munasinghe J, Shapiro E, Koretsky A et al. Noninvasive imaging of the functional effects of anti-VEGF therapy on tumor cell extravasation and regional blood volume in an experimental brain metastasis model. *Clin Exp Metastasis* 2009; 26(5): 403–14. [PubMed: 19277878]
43. Yin J, Liu YN, Tillman H, Barrett B, Hewitt S, Ylaya K et al. AR-regulated TWEAK-FN14 pathway promotes prostate cancer bone metastasis. *Cancer Res* 2014; 74(16): 4306–17. [PubMed: 24970477]
44. Pegoraro G, Misteli T. High-Throughput Imaging for the Discovery of Cellular Mechanisms of Disease. *Trends Genet* 2017; 33(9): 604–615. [PubMed: 28732598]
45. Ewels PA, Peltzer A, Fillinger S, Patel H, Alneberg J, Wilm A et al. The nf-core framework for community-curated bioinformatics pipelines. *Nat Biotechnol* 2020; 38(3): 276–278. [PubMed: 32055031]
46. Lun AT, Chen Y, Smyth GK. It's DE-licious: A Recipe for Differential Expression Analyses of RNA-seq Experiments Using Quasi-Likelihood Methods in edgeR. *Methods Mol Biol* 2016; 1418: 391–416. [PubMed: 27008025]
47. Yu G, Wang LG, Han Y, He QY. clusterProfiler: an R package for comparing biological themes among gene clusters. *OMICS* 2012; 16(5): 284–7. [PubMed: 22455463]

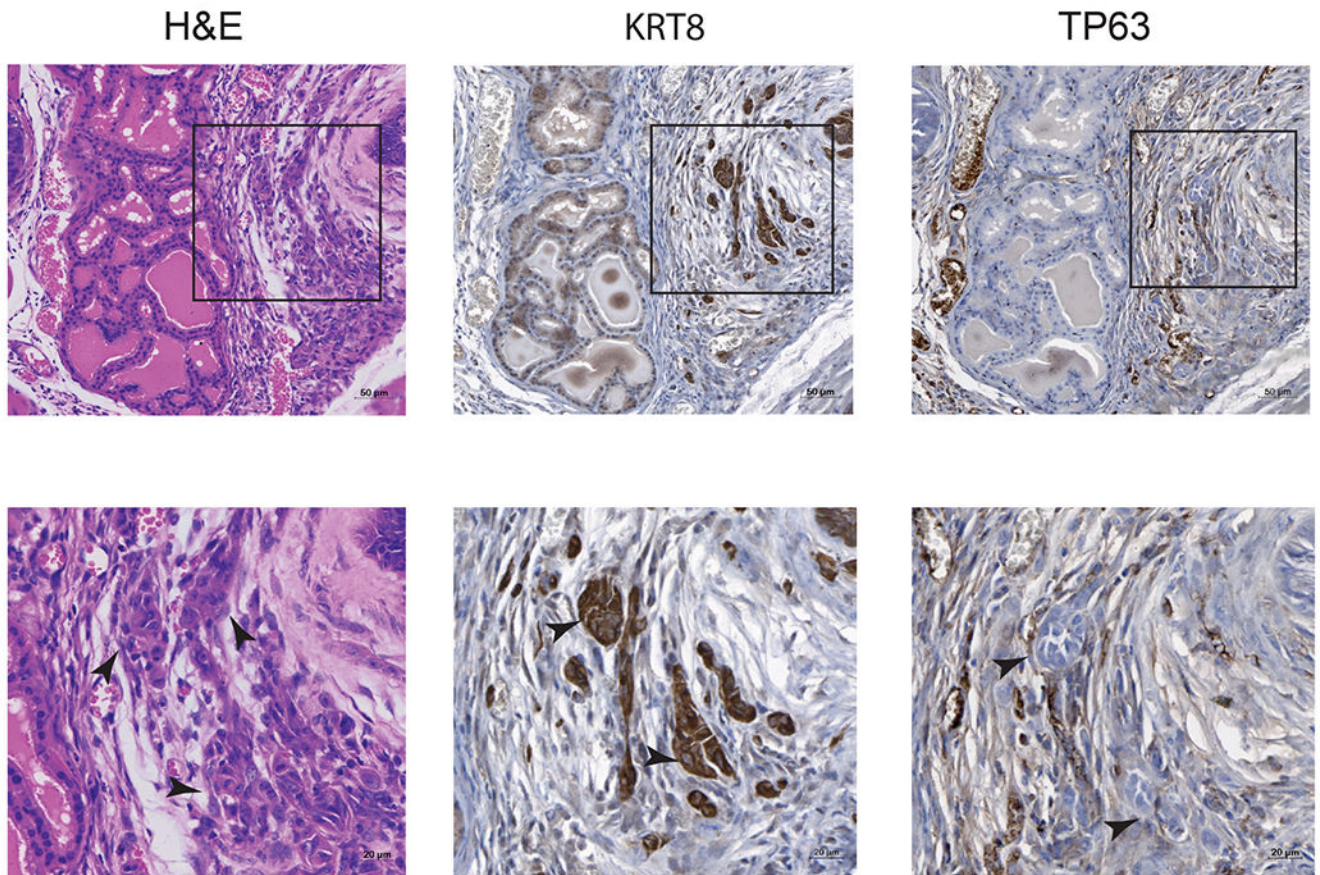


Figure 1: TMPRSS2-ERG synergized with $Kras^{G12D}$ to promote invasive adenocarcinoma in an *in vivo* mouse model. H&E staining and IHC staining for KRT8 and TP63 of tumor nests in TMPRSS-ERG⁺; $Kras^{G12D/+}$; Pb-Cre4⁺ triple transgenic prostates. The scale bars in the figures indicated the power of magnification (see Methods). Arrows indicate tumor nests.

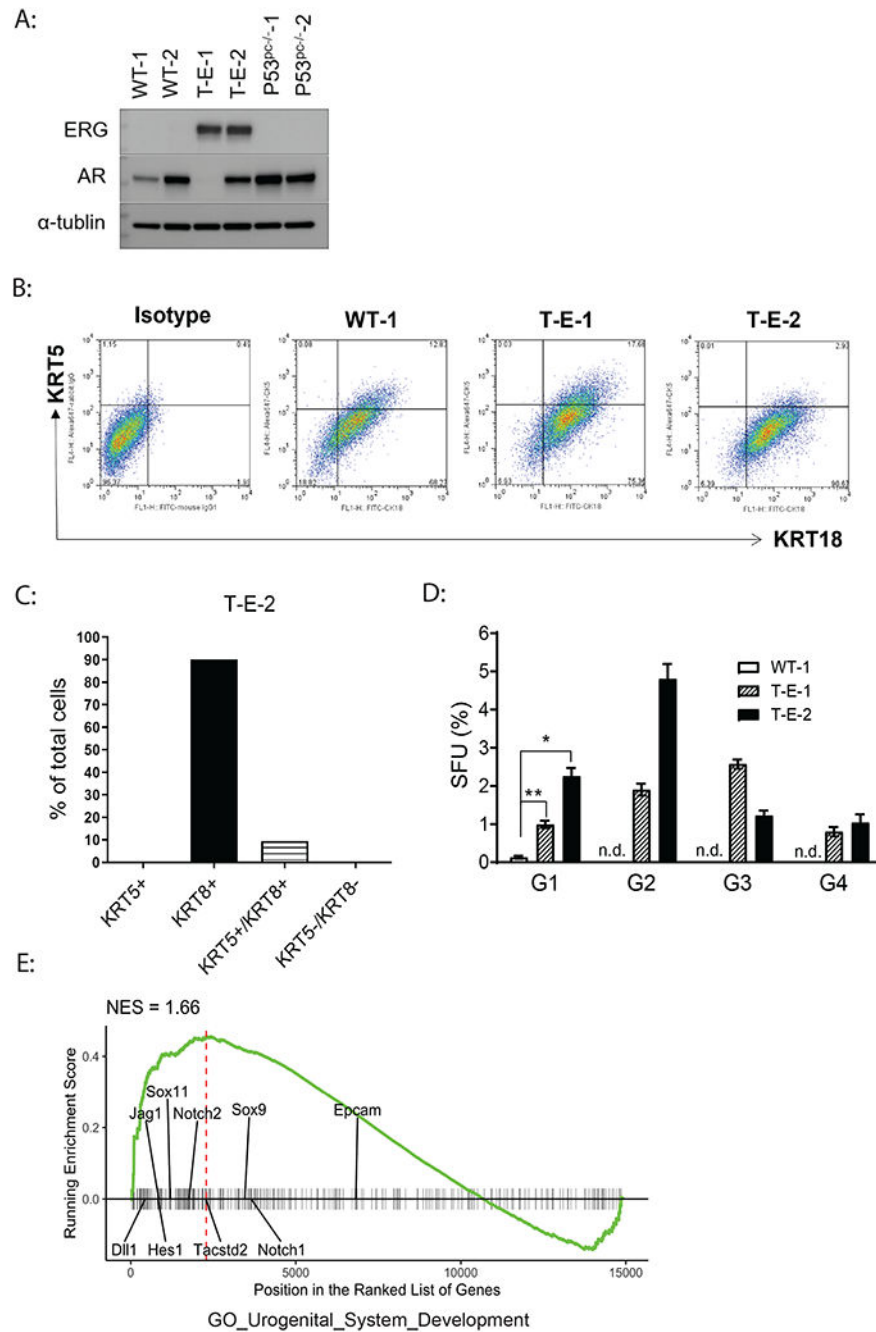


Figure 2: Characterization of primary prostate epithelial cell lines. (A) Western blot showing the expression levels of ERG and AR, (B) FACS staining for intracellular KRT5 and KRT18, (C) Immunofluorescent staining and quantification of KRT5/KRT8 cytokeatin expression in the T-E-2 cell line, (D) Sphere forming assay for WT-1 and T-E-1 & -2 cell lines. Error bars represent \pm SEM, not determined (n.d.). G1 indicates the first generation of spheres derived from the cell lines. G2-G4 refers to the subsequent generations of the serially passaged spheres. All results shown are representative of at least three experiments.

(E) GSEA plot of differentially expressed genes in T-E-2 compared to WT-1 for the GO_Urogenital_System_Development gene set.

Author Manuscript

Author Manuscript

Author Manuscript

Author Manuscript

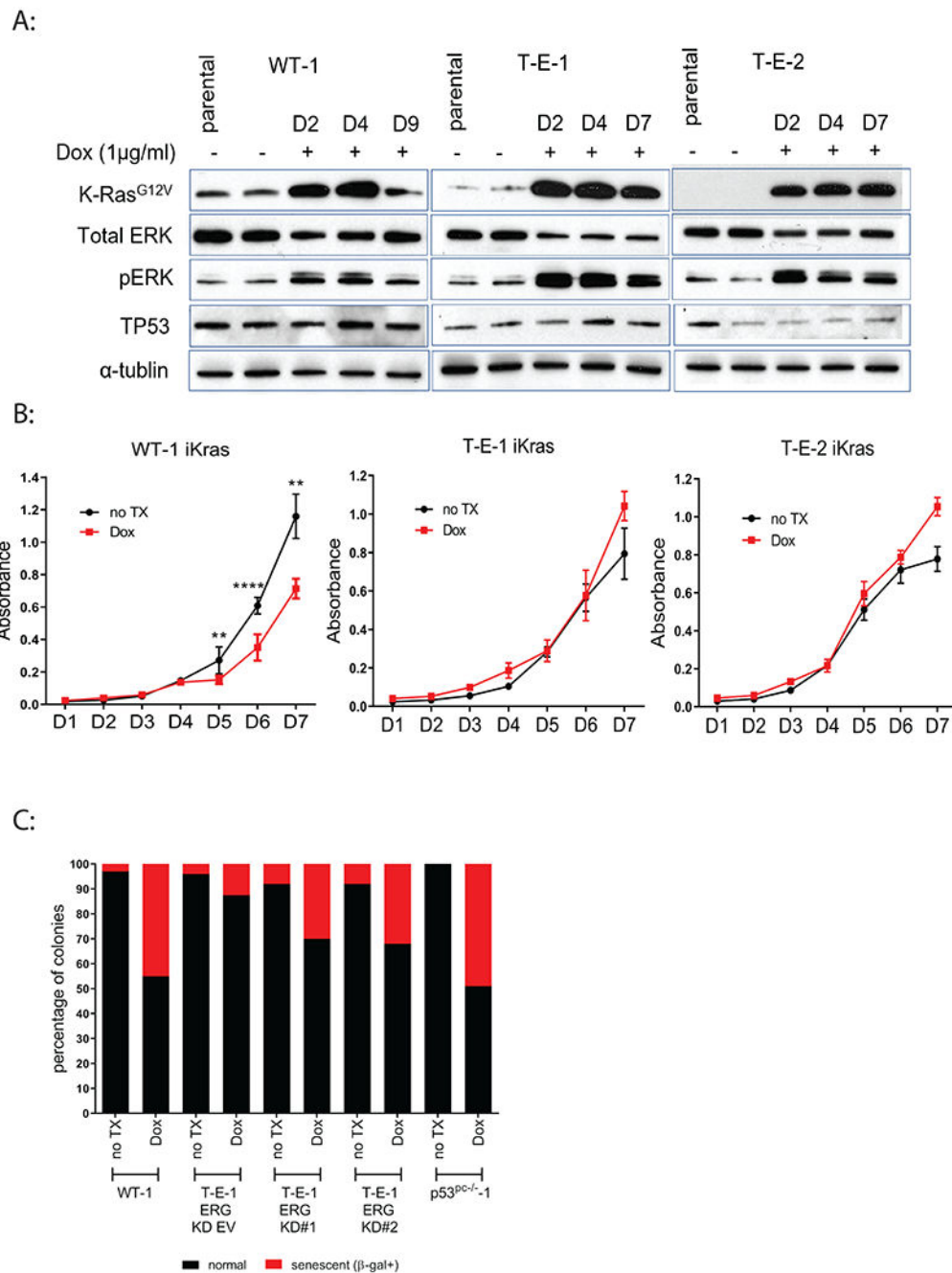


Figure 3: Suppression of Kras^{G12V}-induced senescence by TMPRSS2-ERG. (A) Inducible expression levels of KRAS, pERK, total ERK, and TP53 at different times after doxycycline addition. (B) MTS proliferation assays at various times after doxycycline addition to iKras^{G12V} cell lines, (C) Clonally developed and growing colonies were treated with doxycycline to induce Kras^{G12V} expression for 3 days, followed by staining for senescence associated β-galactosidase. This figure is representative of three independent experiments. T-E-1 ERG

KD#1 and KD#2 indicates lentivirus-mediated ERG shRNA knockdown clones and T-E-1 ERG EV indicates empty vector control clone.

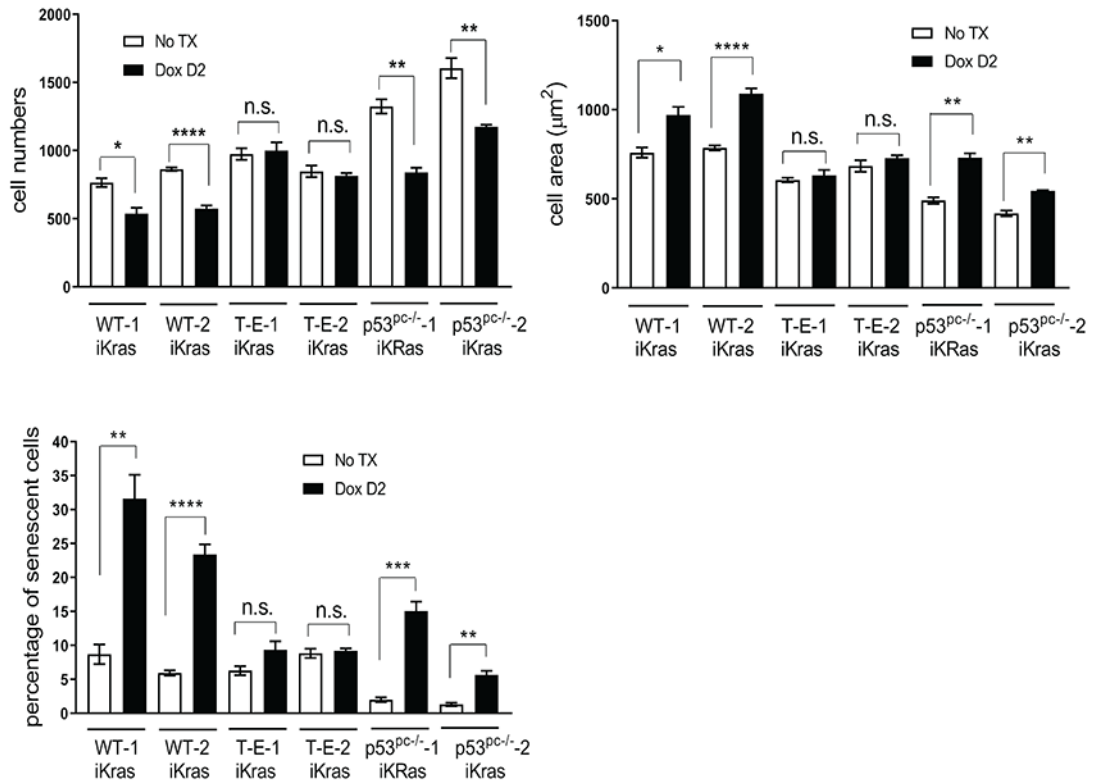
Author Manuscript

Author Manuscript

Author Manuscript

Author Manuscript

A:



B:

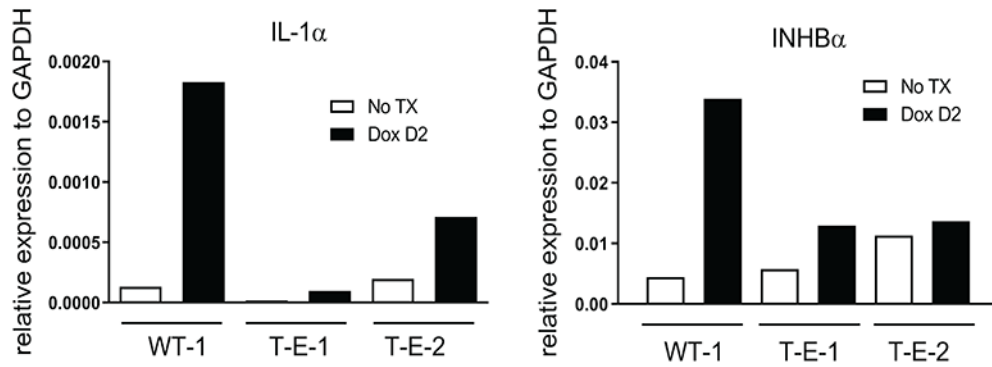


Figure 4:

Suppression of *Kras*^{G12V}-induced senescence by TMPRSS2-ERG. (A) High throughput confocal imaging of *iKras*^{G12V} cells before and 2 days after doxycycline addition quantifying cell number, cell area, and “senescence” as determined by an algorithm that combines seven intracellular and nuclear parameters (see Methods). ****: p<0.0001, ***: p<0.001, **: p<0.01, *: p<0.05, not significant (n.s.) (B) *Il1a* and *Inhba* RNA levels before and after doxycycline addition to the indicated cell lines.

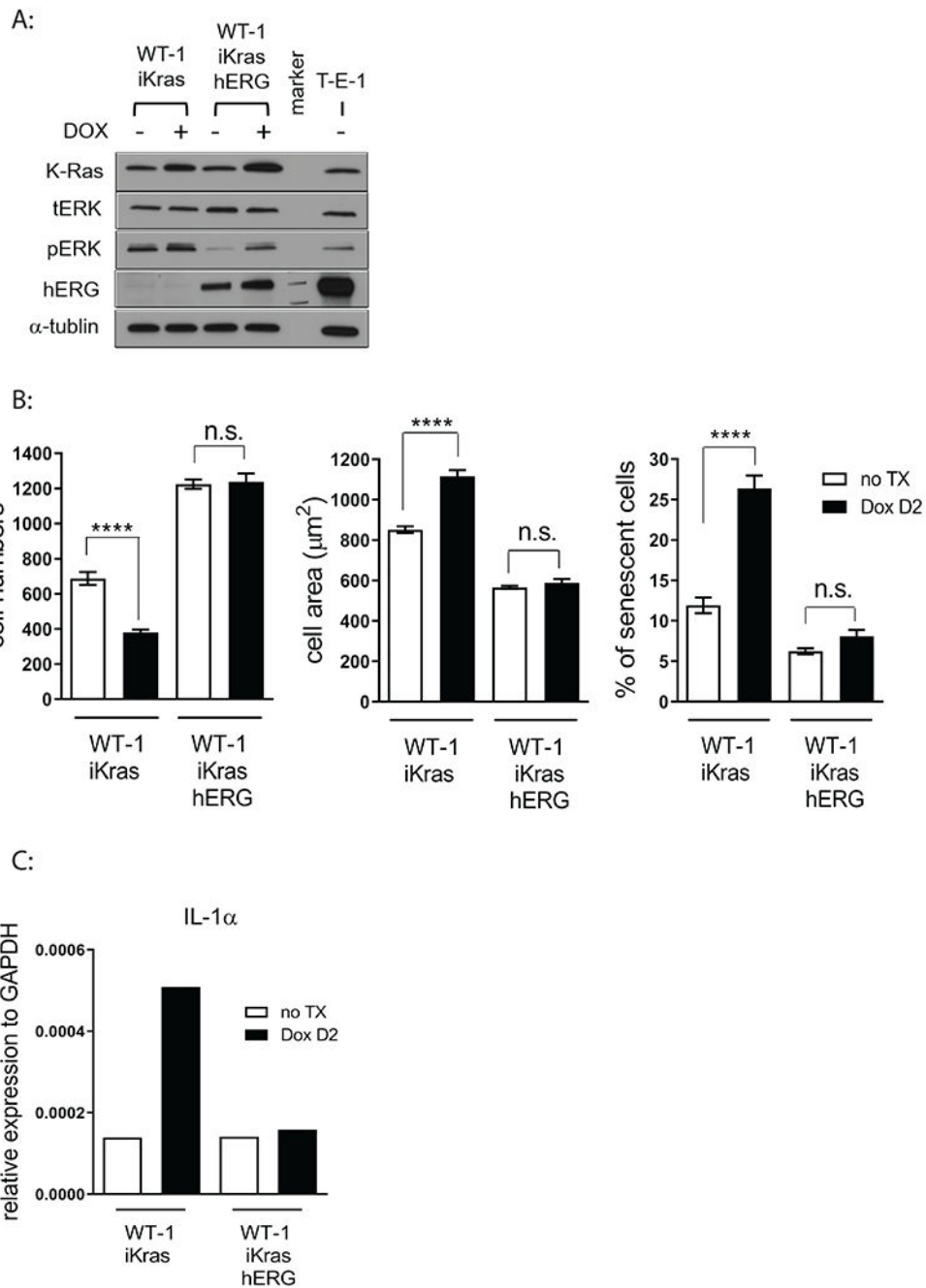


Figure 5: Over-expression of hERG in WT-1 cells reversed *Kras*^{G12V} oncogene-induced senescence. (A) Protein markers in the WT-1 iKras expressing hERG cell line. Senescence parameters following *Kras*^{G12V} induction as determined by (B) high throughput confocal imaging markers and (C) *Il1a* RNA expression; ****: $p < 0.0001$, not significant (n.s.).

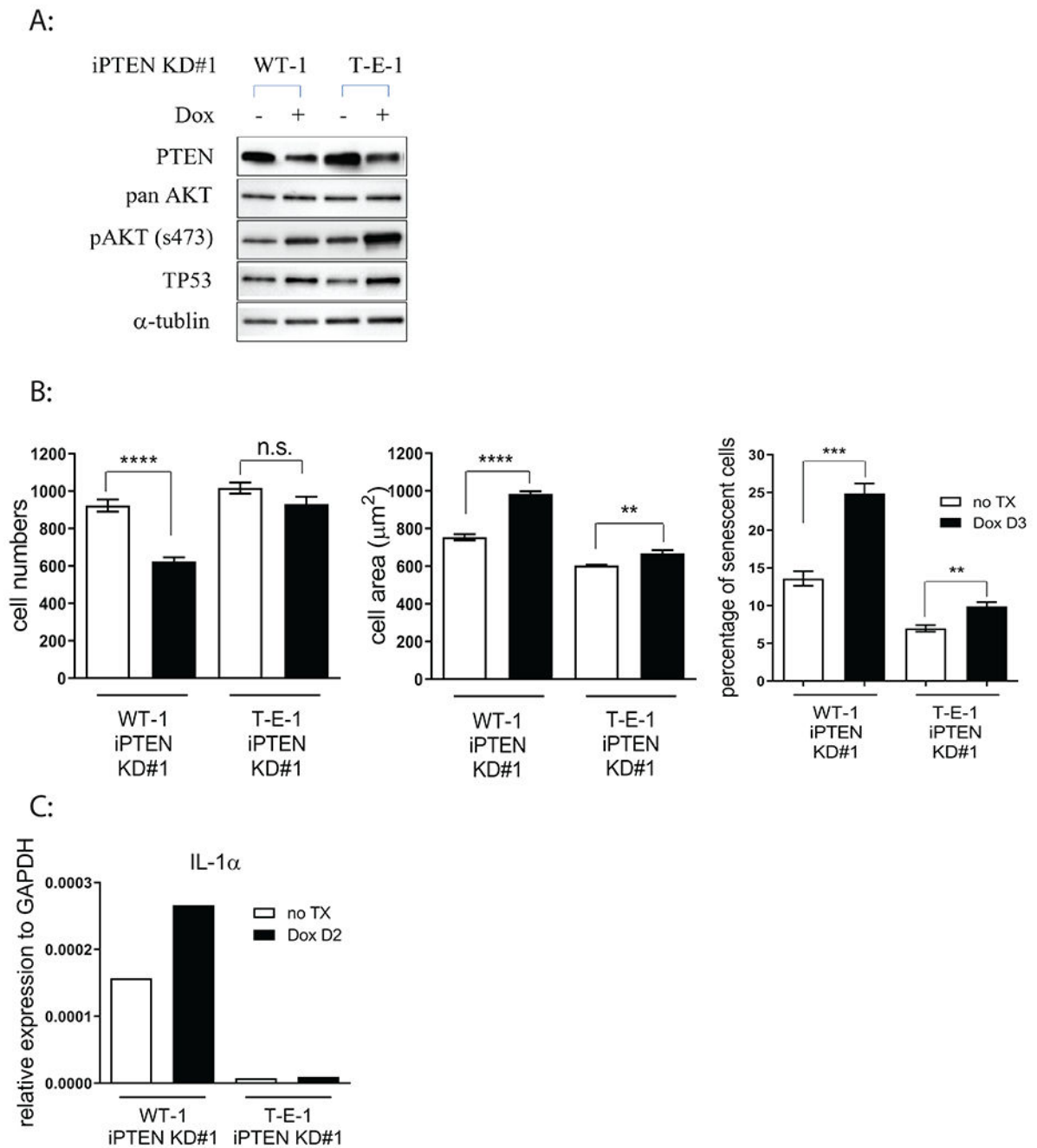


Figure 6: TMPRSS2-ERG expression decreased PTEN depletion-induced senescence. (A) Protein markers in WT-1 and T-E-1 cell lines expressing doxycycline-inducible *Pten* shRNA; senescence parameters 2 days after doxycycline addition as determined by (B) high throughput confocal imaging markers and (C) *Il1a* RNA expression; ****: $p < 0.0001$, ***: $p < 0.001$, **: $p < 0.01$, not significant (n.s.).

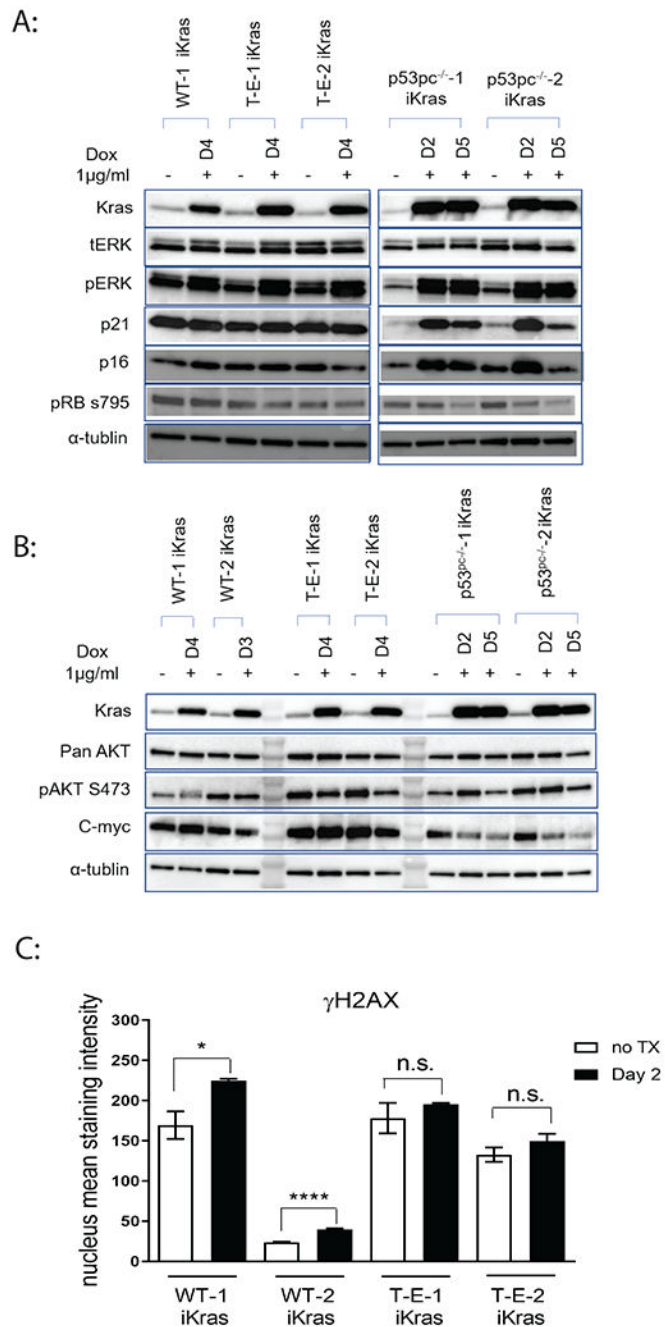


Figure 7: Classical senescence signaling occurs in TP53 null but not in TP53 intact primary prostate luminal epithelial cells. (A & B) Analysis of potential downstream mediators of senescence signaling following oncogenic RAS induction, (C) quantification of DNA damage by γ H2AX staining intensity two days post *Kras*^{G12V} induction.

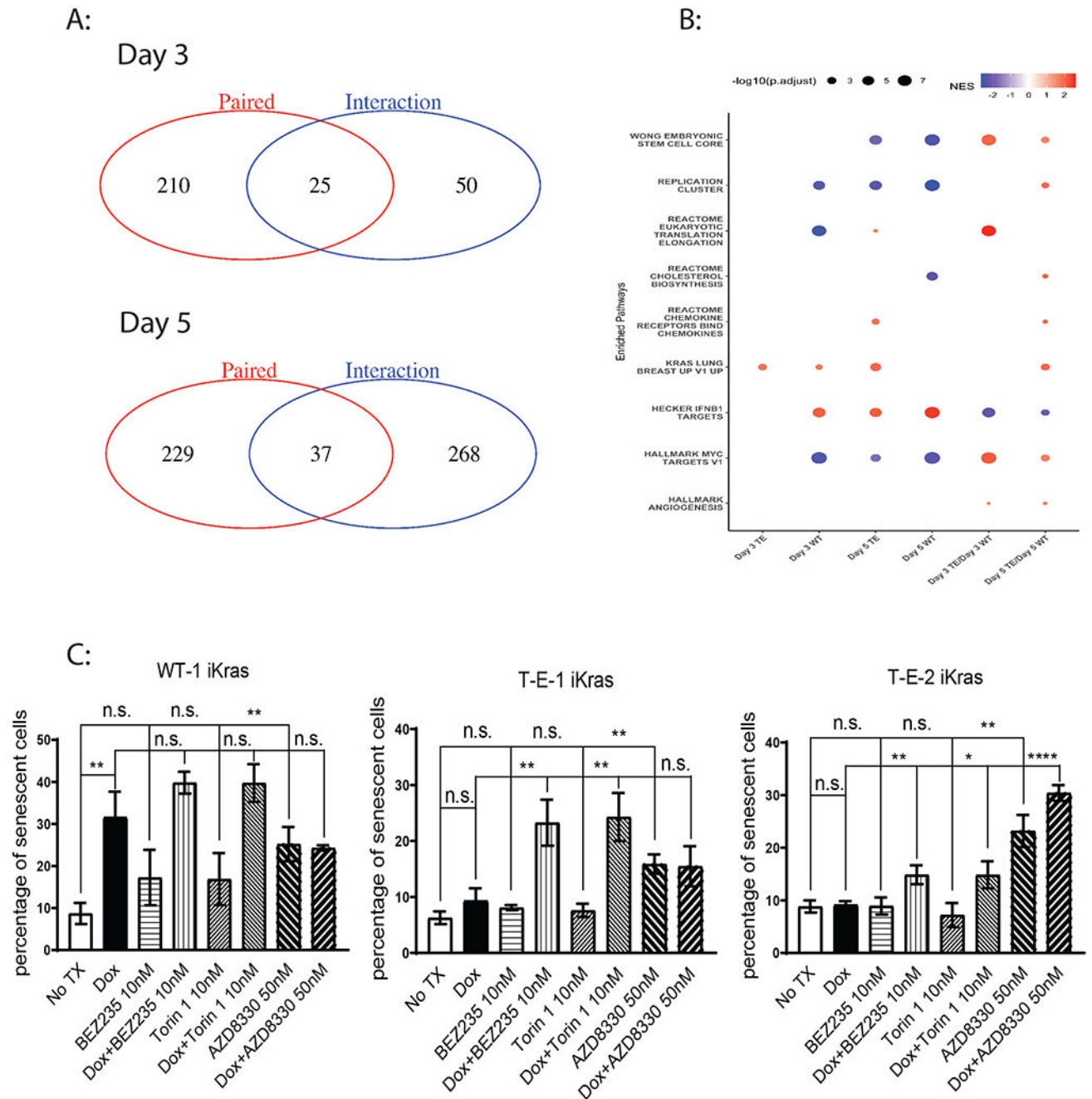


Figure 8:

Bioinformatics analysis of differentially expressed genes in WT-1 iKras^{G12V} and T-E-2 iKras^{G12V} after RAS induction at day 0, day 3 and day 5. (A) Differentially expressed genes (DEGs) were compared in the two models over time for patterns of expression including quantitatively similar (paired) and ERG-specific (interaction) as well as the intersection of the two, in which responses are in the same direction but modulated by ERG. (B) Dot plot summary of GSEA enrichment scores, showing several RAS responsive pathways, for individual cell lines over time as well as the differential expression of the pathway (TE/WT),

(C) High throughput confocal imaging to measure senescence in iKras^{G12V} cells treated with mTORC or MEK/ERK inhibitors simultaneously with RAS induction. BEZ235: PI3K/mTOR inhibitor; Torin 1: mTOR inhibitor; AZD8330: MEK inhibitor

Author Manuscript

Author Manuscript

Author Manuscript

Author Manuscript